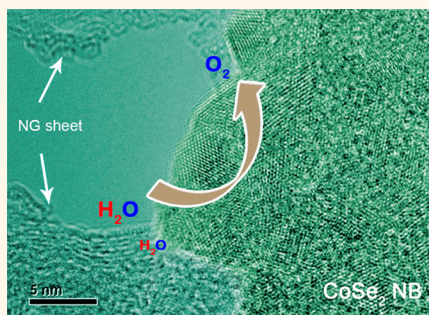


# Nitrogen-Doped Graphene Supported CoSe<sub>2</sub> Nanobelt Composite Catalyst for Efficient Water Oxidation

Min-Rui Gao, Xuan Cao, Qiang Gao, Yun-Fei Xu, Ya-Rong Zheng, Jun Jiang, and Shu-Hong Yu\*

Division of Nanomaterials & Chemistry, Hefei National Laboratory for Physical Sciences at Microscale, Collaborative Innovation Center of Suzhou Nano Science and Technology, Department of Chemistry, University of Science and Technology of China, Hefei 230026, P. R. China

**ABSTRACT** The slow kinetics of the oxygen evolution reaction (OER) greatly hinders the large-scale production of hydrogen fuel from water splitting. Although many OER electrocatalysts have been developed to negotiate this difficult reaction, substantial progresses in the design of cheap, robust, and efficient catalysts are still required and have been considered a huge challenge. Here, we report a composite material consisting of CoSe<sub>2</sub> nanobelts anchored on nitrogen-doped reduced graphene oxides (denoted as NG-CoSe<sub>2</sub>) as a highly efficient OER electrocatalyst. In 0.1 M KOH, the new NG-CoSe<sub>2</sub> catalyst afforded a current density of 10 mA cm<sup>-2</sup> at a small overpotential of mere 0.366 V and a small Tafel slope of ~40 mV/decade, comparing favorably with the state-of-the-art RuO<sub>2</sub> catalyst. This NG-CoSe<sub>2</sub> catalyst also presents better stability than that of RuO<sub>2</sub> under harsh OER cycling conditions. Such good OER performance is comparable to the best literature results and the synergistic effect was found to boost the OER performance. These results raise the possibility for the development of effective and robust OER electrodes by using cheap and easily prepared NG-CoSe<sub>2</sub> to replace the expensive commercial catalysts such as RuO<sub>2</sub> and IrO<sub>2</sub>.



**KEYWORDS:** nitrogen-doped graphene · composite catalysts · water oxidation · cobalt selenides · nanobelts

Conversion of electricity captured from the sustainable but intermittent energy sources (*e.g.*, wind and sunlight) into H<sub>2</sub> fuel by the electrochemical splitting of water is considered one of the holy grails of chemistry.<sup>1,2</sup> However, the oxygen evolution reaction (OER) at the anode suffers from a complex four-electron oxidation process and sluggish kinetics, which imposes considerable electrochemical overpotential ( $\eta$ ) requirements that lead to significant losses to the overall efficiency of water splitting.<sup>3–5</sup> Catalyst development is critical to address this challenge. Current commercial water electrolyzers still rely on the use of ruthenium (Ru) and iridium (Ir) oxides as OER catalysts although their limited availability and high cost.<sup>6,7</sup> As a consequence, the discovery of robust and efficient alternative catalysts that are geologically abundant is highly needed to viable water electrolytic systems.

In recent years, cobalt (Co) has become one of the most popular non-noble metals for the design of robust OER catalysts, including simple<sup>8–13</sup> and mixed-metal oxides,<sup>14–16</sup>

hydro(oxy)oxides,<sup>17</sup> phosphates,<sup>18–23</sup> chalcogenides,<sup>24,25</sup> perovskites,<sup>3,26</sup> and molecular catalysts.<sup>27,28</sup> Besides abundance and low cost, these Co compounds are advantageous for affording water oxidation with moderate overpotentials under neutral or alkaline conditions. More promisingly, numerous studies have shown that, after incorporating other functional materials, the OER performance of the single Co compounds can be greatly optimized.<sup>8,9,13,17,23–25</sup>

For example, Gamelin *et al.* reported the intergration of “Co-Pi” OER catalyst with  $\alpha$ -Fe<sub>2</sub>O<sub>3</sub> can substantially reduce the external power for catalyst's electrolysis chemistry,<sup>23</sup> and the intrinsic reasons for such improvement were proposed by Barroso and co-workers.<sup>29</sup> Jiao and Frei,<sup>8</sup> Yeo and Bell,<sup>9</sup> and Dai *et al.*<sup>13</sup> have developed several remarkable Co<sub>3</sub>O<sub>4</sub>-based OER catalysts by anchoring them on mesoporous silica scaffolds, Au supports, and graphene sheets, respectively. We recently made big efforts to design efficient electrocatalysts<sup>24,30–33</sup> based on a new lamellar mesostructured CoSe<sub>2</sub>/DETA (DETA = diethylenetriamine) nanobelts<sup>34</sup>

\* Address correspondence to shyu@ustc.edu.cn.

Received for review February 13, 2014 and accepted March 20, 2014.

Published online March 20, 2014  
10.1021/nn500880v

© 2014 American Chemical Society

and observed much enhanced OER activity and stability in alkaline solution after modifying them with  $\text{Mn}_3\text{O}_4$  nanoparticles.<sup>24</sup> The synergetic chemical coupling effects between Co compounds and introduced materials was believed to contribute the substantial enhancement. Despite great successes, very few such Co-based catalysts were found to be comparable to or exceed the expensive commercial  $\text{RuO}_2$  and  $\text{IrO}_2$  catalysts.<sup>3</sup>

Graphene sheets (2010 Nobel Physics Prize), are becoming an inexpensive material, have been proven an outstanding matrix to support foreign materials, leading to advanced materials for electrocatalysis and other energy-related applications.<sup>35–38</sup> Considering that, after growing foreign materials onto graphene, the strong chemical and electrical coupling, as well as the possibly optimized electronic structure, can bring significant performance gains,<sup>38</sup> we report here a rationally designed Co-based composite catalyst, *i.e.*, nitrogen-doped reduced graphene/CoSe<sub>2</sub> nanobelts (denoted as NG-CoSe<sub>2</sub> nanobelts), exhibits high OER electrocatalytic performance with low  $\eta$  and small Tafel slope, even comparing favorably with the commercial  $\text{RuO}_2$  catalyst in alkaline medium.

## RESULTS AND DISCUSSION

We selected graphene as substrate by taking advantage of its high electrical conductivity, large surface area, high chemical stability, and mechanical

strength.<sup>38</sup> Through a simple hydrothermal reduction method, ultralong CoSe<sub>2</sub> nanobelts with thin and flexible features could be tightly overlain the graphene sheets (Figure 1 and Supporting Information Figure S1). Such combination can afford the composite catalyst (1) a largely exposed CoSe<sub>2</sub> surfaces as OER active substance in that they are nailed down by NG, preventing undesired aggregates, (2) a high electrical conductivity based on the intimate connection between CoSe<sub>2</sub> nanobelts and NG, and (3) an optimal chemical coupling between the two materials. These merits together endue the NG-CoSe<sub>2</sub> catalyst exceptional OER performance in alkaline solution although pure CoSe<sub>2</sub> only shows small activity and NG is almost OER inactive.

First, large graphene oxide (GO) sheets (Supporting Information, Figure S2) were prepared by oxidation of graphite flakes (Sigma-Aldrich) through the Hummers method,<sup>39</sup> which were then used as supports to provide places for the nucleation and growth of CoSe<sub>2</sub> nanobelts in a closed DETA/H<sub>2</sub>O hydrothermal system (Figure 1a, also see Experimental Section for details of the synthesis). The volume ratio of DETA/H<sub>2</sub>O showed a considerable influence on the morphology of loaded CoSe<sub>2</sub> (Supporting Information, Figure S3), and unique NG-CoSe<sub>2</sub>-nanobelt composite can only be obtained at a ratio of 2:1. Hydrothermal reaction at 180 °C with the presence of suitable amount of DETA led to crystallization of CoSe<sub>2</sub> nanobelts and reduction of GO sheets,

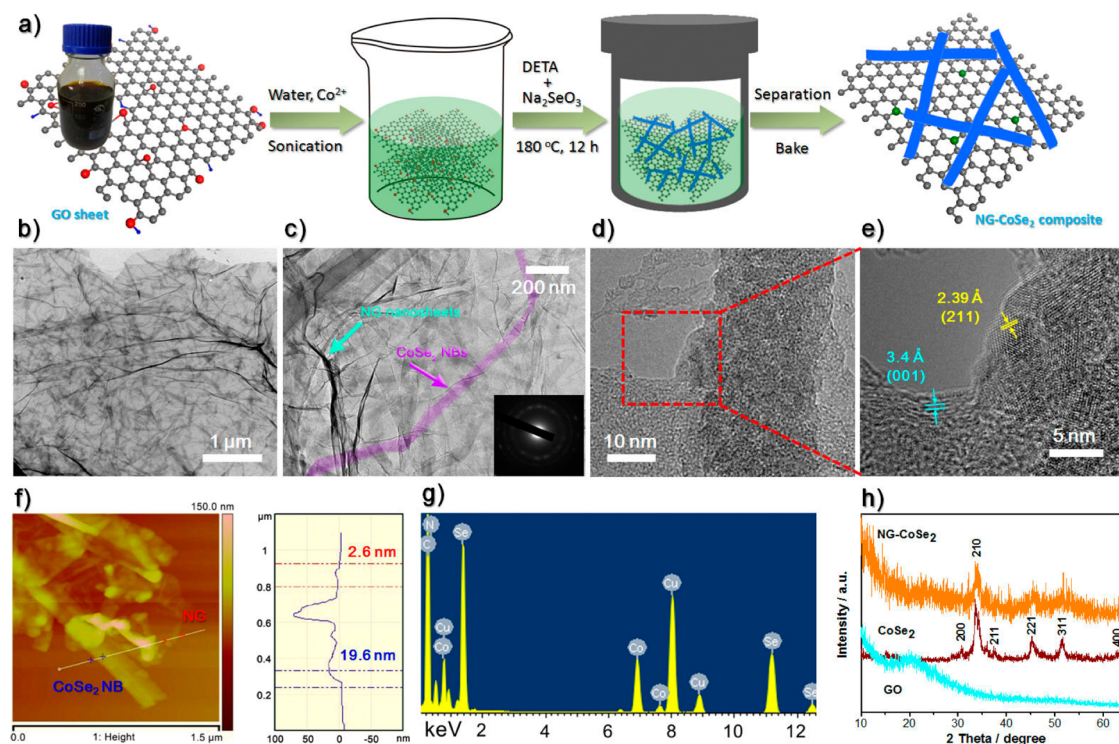


**Figure 1.** (a) Schematic illustration of the formation of the NG-CoSe<sub>2</sub> composite. (b–d) TEM images with different magnifications of NG-CoSe<sub>2</sub> composite. The inset in (c) shows the corresponding SAED pattern. (e) HRTEM image of a part of CoSe<sub>2</sub> nanobelt and its neighboring NG support taken on the marked part in (d). (f) AFM image and corresponding height profile of NG-CoSe<sub>2</sub> composite. (g) EDX spectrum and (h) XRD pattern of the composite catalyst.

forming the fluffy NG-CoSe<sub>2</sub> composite materials. The CoSe<sub>2</sub> loading amount in the composite was about 78.8 wt % based on the thermal-gravimetric measurement (Supporting Information, Figure S4).

Transmission electron microscopy (TEM) images (Figure 1b,c; also Supporting Information Figure S1) clearly show that very long belt-like materials (2–3 μm) with flexible, thin, and almost transparent features are immobilized on large single NG sheets (>6 μm). Selected area electron diffraction shows the polycrystalline nature of the composite, confirming the growth of CoSe<sub>2</sub> nanobelts on NG sheet (inset in Figure 1c and Supporting Information Figure S5). High-resolution TEM (HRTEM) study in Figure 1d,e reveals that the nanobelt surface is coarse and consists of many tiny particles (Supporting Information, Figure S6). The lattice fringe of a representative particle with *d*-spacing of 2.39 Å can be assigned to the (211) plane of the cubic phase CoSe<sub>2</sub> (JCPDS 9-234). Additionally, Figure 1e also discloses the lattice fringe of connected support with a spacing of 3.4 Å, which corresponds well to the (001) plane of graphene.<sup>40</sup> Note here that without GO sheets, the exact same synthesis strategy produced single-crystalline CoSe<sub>2</sub>-DETA mesostructured nanobelts.<sup>34</sup> Such great structural change highlights the important role of GO sheets as a useful substrate for mediating the nucleation and growth of foreign materials. Atomic force microscopy (AFM) was used to characterize the topographic height of NG-CoSe<sub>2</sub> composite on mica (Figure 1f). The height profile in Figure 1f shows average heights of ~19.6 nm for CoSe<sub>2</sub> nanobelt and ~2.6 nm for NG sheet (about 2.6 times higher than single-layer graphene on mica substrate<sup>41</sup>). Energy-dispersive X-ray spectroscopy (EDS) shows that only C, N, Se, and Co can be detected in the composite with Cu peak emanating from the TEM grid (Figure 1g), eliminating other impure elements in the sample. X-ray diffraction (XRD) pattern in Figure 1h further confirms the formation of NG-CoSe<sub>2</sub> composite, which is in line with the above HRTEM analysis.

The surface composition of GO and NG-CoSe<sub>2</sub> composite was characterized by X-ray photoelectron spectroscopy (XPS). Besides the appearance of expected Se and Co elements, the XPS survey spectrum for NG-CoSe<sub>2</sub> clearly reveals that significant content of N (~19.36% atomic percent) is doped in graphene after the small-molecule-amine-assisted hydrothermal process (Figure 2a), in line with our recent work.<sup>42</sup> The high-resolution N 1s spectrum of the NG-CoSe<sub>2</sub> in Figure 2b can be fitted to four peaks of pyridinic N (398.7 eV), C–N–C (399.5 eV), pyrrolic N (400.2 eV), and graphitic N (400.8 eV).<sup>42,43</sup> High-resolution C 1s spectra of pure GO and NG-CoSe<sub>2</sub> composite are compared in Figure 2, panels c and d, which reveal a significant reduction of C–O peak at 286.7 eV, along with the appearance of a new C–N peak at 285.8 eV.<sup>43</sup> Such great changes indicate that the amine-assisted (here is

DETA) hydrothermal strategy is very efficient for the chemical reduction and N doping of GO simultaneously. The reduction of GO is further proved by Fourier transform infrared spectroscopy (FTIR) study shown in Figure 2e, where all the oxygen-containing groups are significantly reduced or entirely removed for the NG-CoSe<sub>2</sub> sample. Raman spectra of GO and NG-CoSe<sub>2</sub> composite all present a D band located around 1342 cm<sup>-1</sup> (arises from the sp<sup>3</sup> defect sites) and a G band around 1570 cm<sup>-1</sup> (arises from sp<sup>2</sup>-bonded pairs) as well as a 2D band located around 2680 cm<sup>-1</sup> and a D + G band around 2910 cm<sup>-1</sup>.<sup>44</sup> Although there is no clear change in the position of D and G bands, the I<sub>D</sub>/I<sub>G</sub> ratio of the NG-CoSe<sub>2</sub> composite did increase notably, suggesting the altered structure of GO originating from the introduction of defects by N-doping.<sup>44</sup>

We then evaluated the electrochemical activity of this new NG-CoSe<sub>2</sub> composite for the OER. To this end, a film of as-synthesized NG-CoSe<sub>2</sub> composite was deposited onto glassy carbon (GC) electrode for cyclic voltammetry (CV) in O<sub>2</sub>-saturated 0.1 M KOH (see Experimental Section for details). As a reference point, similar measurements for commercial Pt/C catalyst (Johnson-Matthey, 20 wt %) and the state-of-the-art RuO<sub>2</sub> catalyst (Sigma-Aldrich) were also performed. The ohmic potential drop (iR) losses that arise from the solution resistance were all corrected (Supporting Information, Figure S7). In Figure 3a, the polarization curve from NG-CoSe<sub>2</sub> composite shows a much earlier OER onset potential (~1.523 V *versus* the RHE) and greater catalytic current than those of pure CoSe<sub>2</sub> nanobelts and Pt/C reference. For RuO<sub>2</sub> catalyst, the OER current appears at a bit smaller onset potential of ~1.481 V (Figure 3a,c, Table 1). In sharp contrast, no obvious voltammetric responses were observed for the bare GC electrode and pure NG sheets (Figure 3a). The physical mixture of NG and CoSe<sub>2</sub> NBs (Supporting Information Figure S8) also exhibits the performance inferior to that of NG-CoSe<sub>2</sub> composite catalyst (Supporting Information Figure S9). It is very meaningful to compare the η requirements for achieving the current density of 10 mA cm<sup>-2</sup>, which is a metric relevant to solar fuel synthesis.<sup>45</sup> Remarkably, the new NG-CoSe<sub>2</sub> composite can afford such current density at a small η of ~0.366 V, equating the η requirement for RuO<sub>2</sub> catalyst, and it is much smaller than those of pure CoSe<sub>2</sub> nanobelts and commercial Pt/C catalyst (Figure 3a,c, Table 1).

The OER kinetics of the above catalysts are probed by corresponding Tafel plots (log *j* – η), as shown in Figure 3b. The resulting Tafel slopes are found to be ~40, ~69, ~66, and ~127 mV dec<sup>-1</sup> for NG-CoSe<sub>2</sub> composite, commercial RuO<sub>2</sub>, pure CoSe<sub>2</sub> nanobelts, and commercial Pt/C, respectively (Figure 3b,c, and Table 1). Note here that NG-CoSe<sub>2</sub> composite exhibits the smallest Tafel slope and is therefore the most

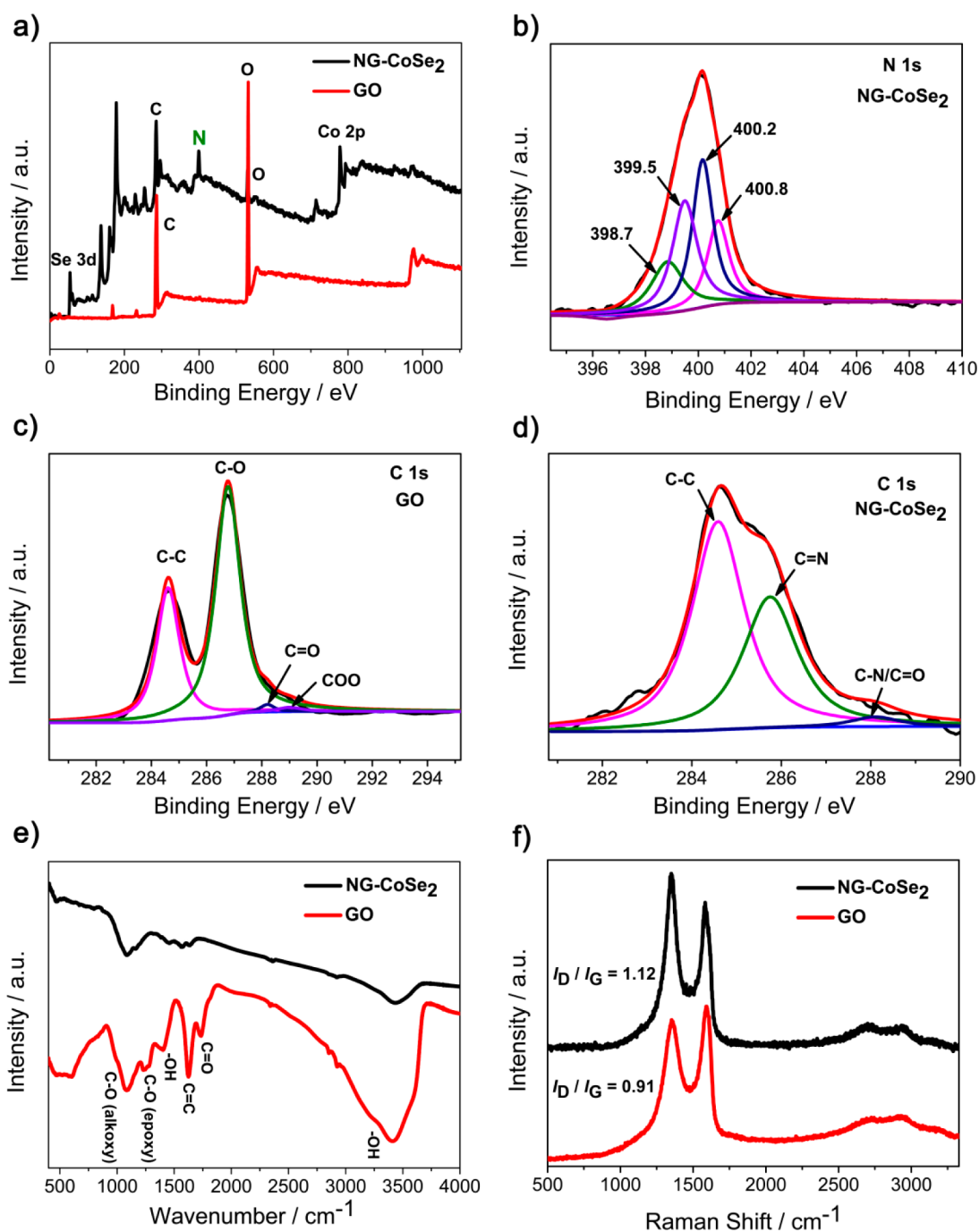


Figure 2. (a) XPS survey spectra of GO and NG-CoSe<sub>2</sub> composite. (b) High-resolution N 1s XPS spectrum of NG-CoSe<sub>2</sub> composite. (c and d) High-resolution C 1s spectra of (c) GO and (d) NG-CoSe<sub>2</sub> composite. (e) FTIR spectra of GO and NG-CoSe<sub>2</sub> composite. (f) Raman spectra of GO and NG-CoSe<sub>2</sub> composite.

efficient electrocatalyst among the studied materials. Such Tafel slope is also smaller than that of the well-investigated Co-based noble metal-free OER catalysts in the literature (Supporting Information, Table S1). It is interesting to note that the Tafel slope of 66 mV dec<sup>-1</sup> for pure CoSe<sub>2</sub> nanobelts is also smaller than that of RuO<sub>2</sub>, suggesting the outstanding intrinsic OER kinetics of this kind of Co-based material even compared with RuO<sub>2</sub> catalyst. The further reduced Tafel slope of kinetic current down to a theoretical value of

40 mV dec<sup>-1</sup> ( $2 \times 2.303RT/3F$ , where  $R$  is the ideal gas constant,  $T$  is the absolute temperature, and  $F$  is the Faraday constant) for NG-CoSe<sub>2</sub> composite demonstrates the synergistic enhancement of OER activity taking effect in the composite.

To further assess their OER catalytic ability, the mass activity and turnover frequency (TOF) of above catalysts at a  $\eta$  of 0.366 V ( $\eta$  that needed to afford a current density of 10 mA cm<sup>-2</sup> for both NG-CoSe<sub>2</sub> composite and RuO<sub>2</sub>) were also presented (Table 1).

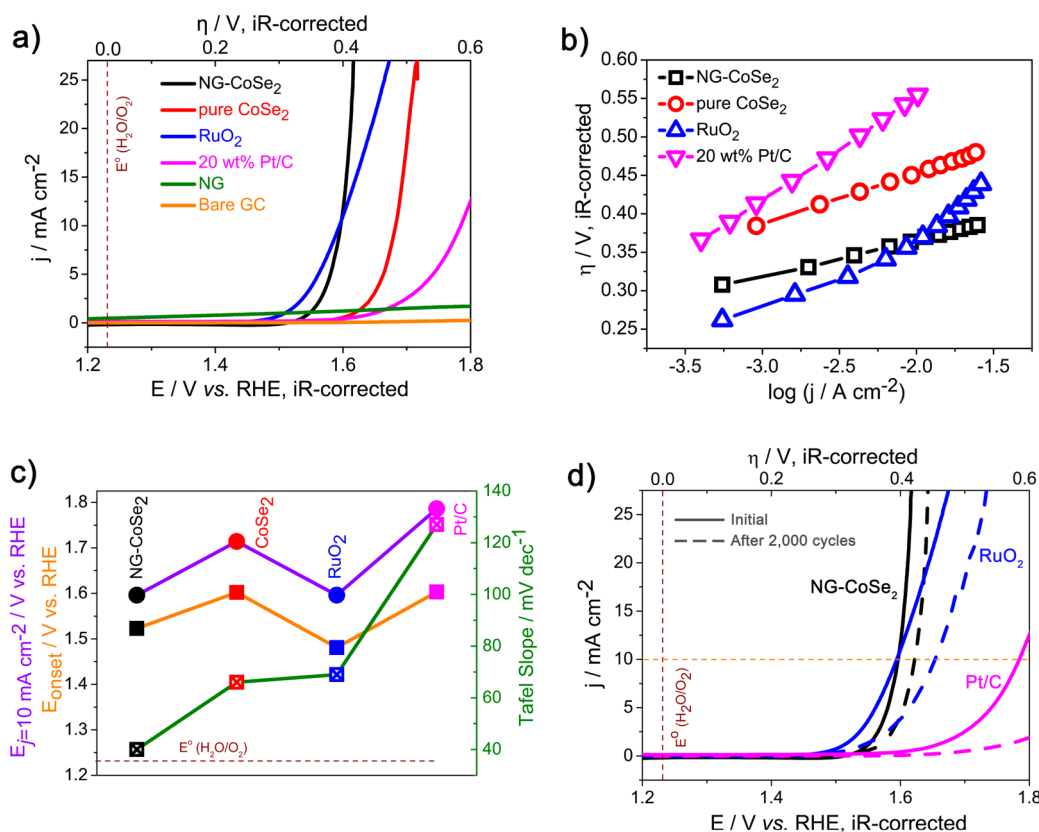


Figure 3. (a) Polarization curves for OER on bare GC electrode and modified GC electrodes comprising the NG sheets, commercial 20 wt % Pt/C and RuO<sub>2</sub> catalysts, pure CoSe<sub>2</sub> nanobelts, and NG-CoSe<sub>2</sub> composite. (b) Tafel plot (overpotential versus log current) derived from (a). (c) Comparison of Tafel slopes, onset potentials, and potentials required to reach  $j = 10 \text{ mA cm}^{-2}$  for NG-CoSe<sub>2</sub> composite, pure CoSe<sub>2</sub> nanobelts, commercial RuO<sub>2</sub>, and 20 wt % Pt/C catalysts. (d) OER polarization curves of NG-CoSe<sub>2</sub> composite, RuO<sub>2</sub>, and 20 wt % Pt/C catalysts before and after potential sweeps (0.3–0.8 V versus Ag/AgCl) for 2000 cycles. All the measurements were performed in O<sub>2</sub>-saturated 0.1 M KOH (pH  $\sim$  13) at 5 mV s<sup>-1</sup> scan rate at 1600 rpm. The iR loss from the solution resistance was corrected. Catalyst loading:  $\sim$ 0.2 mg cm<sup>-2</sup>.

TABLE 1. Comparison of OER Activity Data for Different Catalysts

catalyst	onset potential [V vs. RHE]	$\eta$ @ $J = 10 \text{ mA cm}^{-2}$ [mV]	mass activity @ $\eta = 366 \text{ mV}$ [ $\text{A g}^{-1}$ ]	Tafel slope [ $\text{mV dec}^{-1}$ ]	TOF @ $\eta = 366 \text{ mV}$ [ $\text{s}^{-1}$ ] <sup>a</sup>
NG-CoSe <sub>2</sub>	1.523	366	63.45 <sup>b</sup>	40	0.03565 <sup>b</sup>
CoSe <sub>2</sub>	1.602	484	2.75	66	0.00773
RuO <sub>2</sub>	1.481	366	50.00	69	0.01724
20 wt % Pt/C	1.603	556	9.86 <sup>c</sup>	127	0.00505 <sup>c</sup>

<sup>a</sup> The values of TOF were calculated by assuming that every metal atom are involved in the catalysis (lower bound, see Experimental Section for the calculated method).

<sup>b</sup> Based on the amount of CoSe<sub>2</sub> (78.8 wt %). <sup>c</sup> Based on the amount of Pt (20 wt %).

The calculated mass activity for NG-CoSe<sub>2</sub> composite is 63.45 A g<sup>-1</sup>, outperforming other studied catalysts even RuO<sub>2</sub> (Table 1). The intrinsic activities of above catalysts were estimated by TOF. The constructed new NG-CoSe<sub>2</sub> composite was found to exhibit the highest TOF of  $\sim 3.565 \times 10^{-2} \text{ s}^{-1}$  on the assumption that every metal atom catalytically active (lower bound, Table 1).

Other than high activity, the long-term stability is another critical parameter that determines the practicability of electrocatalysts. To assess this, we performed continuous potential cycling between 1.26 and 1.76 V (versus RHE) for the NG-CoSe<sub>2</sub> composite with RuO<sub>2</sub> and Pt/C as references in O<sub>2</sub>-saturated 0.1 M KOH. As shown in Figure 3d, after 2000 cycles, the NG-CoSe<sub>2</sub>

catalyst needs a mere 25 mV increase in  $\eta$  to reach the current density of 10 mA cm<sup>-2</sup>, while the same experiment leads to a 58 mV  $\eta$  increase for RuO<sub>2</sub> and a failure to reach such current density for Pt/C, demonstrating the superior durability of the new NG-CoSe<sub>2</sub> composite catalyst.

As noted above, pure N-doped graphene did not affect OER activity (Figure 3a). Therefore, it stands to reason that the exceptional OER activity of NG-CoSe<sub>2</sub> composite was originated from loaded CoSe<sub>2</sub> nanobelts, where NG served as a synergist. For well-studied cobalt oxides, it has been widely accepted that Co (IV) cations are critical to enable OER.<sup>9,12</sup> The high valent Co cations were believed to enhance the electrophilicity

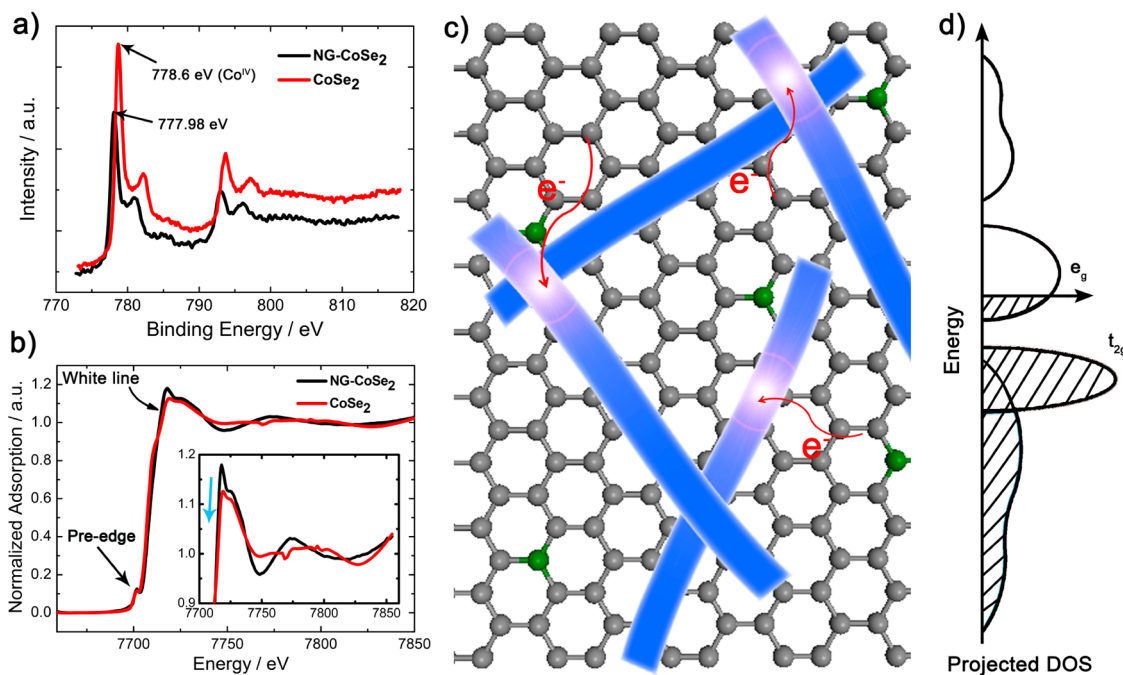


**Figure 4.** (a) High-resolution Co 2p XPS spectra for pure CoSe<sub>2</sub> nanobelts and NG-CoSe<sub>2</sub> composite. (b) Co K-edge XANES spectra for pure CoSe<sub>2</sub> nanobelts and NG-CoSe<sub>2</sub> composite. Inset in (b) is the enlarged region of peaks of Co K-edge XANES white line. (c) Schematic image demonstrates the electron donation from the NG to CoSe<sub>2</sub>. Gray, green balls and blue belts correspond to C, N atoms and CoSe<sub>2</sub> nanobelts, respectively. (d) Schematic density-of-states (DOS) of CoSe<sub>2</sub>, which is adapted from ref 50.

of adsorbed O, thus facilitate the formation of hydroperoxy (OOH) species and subsequent conversion to O<sub>2</sub> molecules.<sup>9,12</sup> As to cubic phase CoSe<sub>2</sub>, the surface Co (IV) cations (verified by the binding energy of Co 2p<sub>3/2</sub> at 778.6 eV, Figure 4a) were also be proven to the cause of its observed OER activity.<sup>24</sup> However, the metal–oxygen interaction is not optimum. On the basis of the *d*-band theory, the catalytic activity of a material is in principle determined by the metal *d* states near the Fermi level.<sup>46</sup> For transition metal chalcogenides, the interaction between oxygen and metal *d* states is responsible for the OER activity. Because the e<sub>g</sub> orbital of transition metal ions participates in  $\sigma$ -bonding with a surface-anion adsorbate, modulating the *d*-electron filling in e<sub>g</sub> bands will optimize the bond strength of oxygen-related intermediate species (important for OER) on catalytic surface and thus foster performance optimization.<sup>3</sup> The greatly improved OER performance of CoSe<sub>2</sub> nanobelts after growing on graphene indicates the modified electronic structure of CoSe<sub>2</sub> in the composite materials, which were gleaned by X-ray photoelectron spectroscopy (XPS) and X-ray absorption near edge spectra (XANES) measurements (Figure 4). Compared to pure CoSe<sub>2</sub> nanobelts, the electron binding energy of Co 2p for NG-CoSe<sub>2</sub> composite showed a  $\sim$ 0.62 eV decrease, corresponding to electron transfer from NG to CoSe<sub>2</sub> (Figure 4a,c).<sup>47</sup> Such electron donation was also confirmed by XANES. Figure 4b and the inset show the normalized XANES spectra collected at Co K-edge,

from which we can see an obvious increase in white line intensity after growing CoSe<sub>2</sub> on NG sheets, strongly indicating the electron transfer from NG to CoSe<sub>2</sub> (Figure 4c).<sup>48,49</sup> As to the partially filled e<sub>g</sub> bands (e<sub>g</sub> < 1) of pyrite-type CoSe<sub>2</sub>,<sup>50</sup> the surface-oxygen interaction is a bit strong for OER (Figure 4d). The electron donation from NG sheets to CoSe<sub>2</sub> will afford more e<sub>g</sub>-filling in CoSe<sub>2</sub>, which could weaken the surface-oxygen interaction to moderate bond strength (neither too strong nor too weak), thus greatly enhancing the OER kinetics. The optimized electronic structure of CoSe<sub>2</sub> after growing them on NG that leads to the improved OER activity can also be evidenced by the inferior performance of their physically mixed sample (Supporting Information Figures S8 and S9). Moreover, the NG sheets also endue the constructed composite catalyst with a high electrical conductivity. These advantages in the composite together are responsible for the synergistic OER catalytic activity.

## CONCLUSIONS

In summary, we have successfully grown *in situ* CoSe<sub>2</sub> nanobelts on GO sheets to prepare a new N-doped graphene/CoSe<sub>2</sub> composite catalyst by using a simple small-molecule-amine-assisted hydrothermal strategy. This cheap and easily prepared electrocatalyst showed exceptional OER activity with a small  $\eta$  of 0.366 V at the current density of 10 mV cm<sup>-2</sup>, large anodic currents, and a Tafel slope down to 40 mV dec<sup>-1</sup> in alkaline solution, which was found to approach or

compare favorably with the best performance of well-studied Co-based materials and the commercial RuO<sub>2</sub> catalyst. The NG-CoSe<sub>2</sub> catalyst also exhibited outstanding durability under harsh OER cycling conditions. The synergism between the N-doped reduced graphene and

CoSe<sub>2</sub> nanobelts is believed to boost the excellent OER performance. Our study raises great promises for designing effective OER electrocatalysts by suitable electrical and chemical coupling of cheap functional materials, which is highly request for a viable hydrogen economy.

## EXPERIMENTAL SECTION

**Materials.** All chemicals are of analytical grade and were used as received without further purification.

**Synthesis of Graphene Oxide (GO) Sheets.** GO was prepared by chemical oxidation and exfoliation of graphite flakes (Sigma-Aldrich) under acidic conditions according to the Hummers' method.<sup>39</sup> The obtained GO was washed thoroughly and redispersed in deionized water (DIW) to harvest final GO DIW suspension with a concentration of ~0.3 mg mL<sup>-1</sup> (the concentration of the GO stock suspension was determined by measuring the mass of the GO lyophilized from a given volume of the suspension).

**Synthesis of NG-CoSe<sub>2</sub> Composite.** In a typical procedure, 1 mmol (0.249 g) of Co(AC)<sub>2</sub>·H<sub>2</sub>O was added into 13 mL of GO DIW suspension under magnetic stirring. About 10 min later, 26 mL of DETA (diethylenetriamine) and 1 mmol (0.173 g) of Na<sub>2</sub>SeO<sub>3</sub> were added. After further stirring for 0.5 h in a beaker to dissolve completely, the homogeneous solution was transferred into a 50 mL Teflon-lined autoclave, which was sealed and maintained at 180 °C for 12 h and then naturally cooled to room temperature. The resulting solid product was collected and washed with DIW. Then, the nanocomposite powder was obtained by freeze-drying for next characterizations.

**Synthesis of N-Doped Reduced Graphene (NG) and Pure CoSe<sub>2</sub> Nanobelts.** The synthetic procedure of NG is the same with that for preparing NG-CoSe<sub>2</sub>, the only difference is that no Co(AC)<sub>2</sub>·H<sub>2</sub>O and Na<sub>2</sub>SeO<sub>3</sub> were added during the synthesis. Pure CoSe<sub>2</sub> nanobelts were also made through the same procedures as preparing NG-CoSe<sub>2</sub>, the only difference is that GO DIW suspension was replaced by pure DIW.

**Materials Characterization.** The samples were characterized by different analytic techniques. X-ray powder diffraction (XRD) was carried out on a Rigaku D/max-rA X-ray diffractometer with Cu K $\alpha$  radiation ( $\lambda = 1.54178 \text{ \AA}$ ); TEM images, HRTEM images, selected-area electron diffraction (SAED), and an Energy-disperse X-ray spectrum (EDS) were taken with a JEOJ-2010 transmission electron microscope with an acceleration voltage of 200 kV. An atomic force microscope (Nanoscope IIIa; Digital Instruments) was used to measure the morphology of the sample. A Si tip (Nanoprobes, Digital Instruments, Inc.) was used in the tap mode. The X-ray photoelectron spectra (XPS) were recorded on an ESCALab MKII X-ray photoelectron spectrometer using Mg K $\alpha$  radiation exciting source. The Fourier transform infrared (FTIR) spectra were measured on a Bruker Vector-22 FT-IR spectrometer at room temperature. Raman spectroscopy was carried out on a JY LABRAM-HR confocal laser micro-Raman spectrometer using Ar<sup>+</sup> laser excitation with a wavelength of 514.5 nm. Thermal gravimetric analysis (TGA) was carried out on a Perkin-Elmer Diamond TG/DTA thermal analyzer with a heating rate of 10 °C · min<sup>-1</sup> · Pa<sup>-1</sup> and a flowing N<sub>2</sub> of 50 mL · min<sup>-1</sup> · Pa<sup>-1</sup>.

**Electrocatalytic Study.** Electrochemical measurements were performed at room temperature using a rotating disk working electrode made of glassy carbon (PINE, 5 mm diameter, 0.196 cm<sup>2</sup>) connected to a Multipotentiostat (IM6ex, ZAHNER elektrik, Germany). The glassy carbon electrode was polished to a mirror finish (No. 40-6365-006, Gamma Micro Polish Alumina, Buehler; No.40-7212, Microcloth, Buehler) and thoroughly cleaned before use. Pt wire and Ag/AgCl (PINE, 4 M KCl) were used as counter and reference electrodes, respectively. The potentials reported in our work were *versus* the reversible hydrogen electrode (RHE) through RHE calibration described below.

The preparation method of the working electrodes containing investigated catalysts can be found as follows. In short, 5 mg

of catalyst powder was dispersed in 1 mL of 3:1 (v/v) DIW/2-propanol mixed solvent with 40  $\mu$ L of Nafion solution (5 wt %, Sigma-Aldrich), and then the mixture was ultrasonicated for about 1 h to generate a homogeneous ink. Next, 8  $\mu$ L of the dispersion was transferred onto the glassy carbon disk, leading to the catalyst loading ~0.2 mg cm<sup>-2</sup>. Finally, the as-prepared catalyst film was dried at room temperature. For comparison, bare glassy carbon electrode which has been polished and cleaned was also dried for electrochemical measurement.

Before the electrochemical measurement, the electrolyte (0.1 M KOH, 99.99% metal purity, pH ~13) was degassed by bubbling oxygen for at least 30 min to ensure the H<sub>2</sub>O/O<sub>2</sub> equilibrium at 1.23 V *versus* RHE at a rotation rate of 1600 rpm. The polarization curves were obtained by sweeping the potential from 0 to 1 V *versus* Ag/AgCl at room temperature and 1600 rpm, with a sweep rate of 5 mV s<sup>-1</sup>. The cyclic voltammetry (CV) curves were obtained by sweeping the potential from -0.2 to 1 V *versus* Ag/AgCl at room temperature and 1600 rpm. All the data were recorded after applying a number of potential sweeps until which were stable.

The accelerated stability tests were performed in O<sub>2</sub>-saturated 0.1 M KOH at room temperature by potential cycling between 0.3 and 0.8 V *versus* Ag/AgCl at a sweep rate of 100 mV/s for 2000 cycles. At the end of the cycles, the resulting electrodes were used for polarization curves at a sweep rate of 5 mV/s.

**RHE Calibration.** In all measurements, we used Ag/AgCl (PINE, 4 M KCl) as the reference electrode. It was calibrated with respect to RHE. The calibration was performed in the high purity hydrogen saturated electrolyte with a Pt foil as the working electrode. Cyclic voltammetry (CV) was run at a scan rate of 1 mV s<sup>-1</sup>, and the average of the two potentials at which the current crossed zero was taken to be the thermodynamic potential for the hydrogen electrode reaction. In 0.1 M KOH solution,  $E_{\text{RHE}} = E_{\text{Ag/AgCl}} + 0.96 \text{ V}$ .

**Calculation method.** Details concerning the calculation of mass activity and turnover frequency (TOF) are shown below:

The values of mass activity (A g<sup>-1</sup>) were calculated from the catalyst loading  $m$  (0.2 mg cm<sup>-2</sup>) and the measured current density  $j$  (mA cm<sup>-2</sup>) at  $\eta = 0.336 \text{ V}$ :

$$\text{Mass activity} = \frac{j}{m} \quad (1)$$

The values of TOF were calculated by assuming that every metal atom is involved in the catalysis (lower TOF limits were calculated):

$$\text{TOF} = \frac{j \times S}{4 \times F \times n} \quad (2)$$

Here,  $j$  (mA cm<sup>-2</sup>) is the measured current density at  $\eta = 0.336 \text{ V}$ ,  $S$  (0.196 cm<sup>2</sup>) is the surface area of glassy carbon disk, the number 4 means 4 electrons/mol of O<sub>2</sub>,  $F$  is Faraday's constant (96485.3 C mol<sup>-1</sup>), and  $n$  is the moles of coated metal atom on the electrode calculated from  $m$  and the molecular weight of the coated catalysts.

**Conflict of Interest:** The authors declare no competing financial interest.

**Acknowledgment.** We acknowledge the special funding support from the Ministry of Science and Technology of China, the National Basic Research Program of China (2012BAD32B05-4, 2010CB934700, 2013CB933900, 2014CB931800), the National Natural Science Foundation of China (Grants 91022032,

91227103, 21061160492, J1030412, 21101051), the Chinese Academy of Sciences (Grant KJZD-EWM01-1), the Fundamental Research Funds for the Central Universities (2012HGXC0003, WK 2060190021), and the Principal Investigator Award by the National Synchrotron Radiation Laboratory at the University of Science and Technology of China.

**Supporting Information Available:** additional TEM and HRTEM images, TGA curve, and iR-correction. This material is available free of charge via the Internet at <http://pubs.acs.org>.

## REFERENCES AND NOTES

- Cook, T. R.; Dogutan, D. K.; Reece, S. Y.; Surendranath, Y.; Teets, T. S.; Nocera, D. G. Solar Energy Supply and Storage for the Legacy and Non Legacy Worlds. *Chem. Rev.* **2010**, *110*, 6474–6502.
- Walter, M. G.; Warren, E. L.; McKone, J. R.; Boettcher, S. W.; Mi, Q. X.; Santori, E. A.; Lewis, N. S. Solar Water Splitting Cells. *Chem. Rev.* **2010**, *110*, 6446–6473.
- Suntivich, J.; May, K. J.; Gasteiger, H. A.; Goodenough, J. B.; Shao-Horn, Y. A Perovskite Oxide Optimized for Oxygen Evolution Catalysis from Molecular Orbital Principles. *Science* **2011**, *334*, 1383–1385.
- McAlpin, J. G.; Stich, T. A.; Casey, W. H.; Britt, R. D. Comparison of Cobalt and Manganese in the Chemistry of Water Oxidation. *Coord. Chem. Rev.* **2012**, *256*, 2445–2452.
- Dau, H.; Limberg, C.; Reier, T.; Risch, M.; Roggan, S.; Strasser, P. The Mechanism of Water Oxidation: From Electrolysis via Homogeneous to Biological Catalysis. *ChemCatChem* **2010**, *2*, 724–761.
- Rossmel, J.; Qu, Z. W.; Zhu, H.; Kroes, G. J.; Norskov, J. K. Electrolysis of Water on Oxide Surfaces. *J. Electroanal. Chem.* **2007**, *607*, 83–89.
- Lee, Y.; Suntivich, J.; May, K. J.; Perry, E. E.; Shao-Horn, Y. Synthesis and Activities of Rutile IrO<sub>2</sub> and RuO<sub>2</sub> Nanoparticles for Oxygen Evolution in Acid and Alkaline Solutions. *J. Phys. Chem. Lett.* **2012**, *3*, 399–404.
- Jiao, F.; Frei, H. Nanostructured Cobalt Oxide Clusters in Mesoporous Silica as Efficient Oxygen-Evolving Catalysts. *Angew. Chem., Int. Ed.* **2009**, *48*, 1841–1844.
- Yeo, B. S.; Bell, A. T. Enhanced Activity of Gold-Supported Cobalt Oxide for the Electrochemical Evolution of Oxygen. *J. Am. Chem. Soc.* **2011**, *133*, 5587–5593.
- Wee, T. L.; Sherman, B. D.; Gust, D.; Moore, A. L.; Moore, T. A.; Liu, Y.; Scaiano, J. C. Photochemical Synthesis of a Water Oxidation Catalyst Based on Cobalt Nanostructures. *J. Am. Chem. Soc.* **2011**, *133*, 16742–16745.
- Esswein, A. J.; McMurdo, M. J.; Ross, P. N.; Bell, A. T.; Tilley, T. D. Size-Dependent Activity of Co<sub>3</sub>O<sub>4</sub> Nanoparticle Anodes for Alkaline Water Electrolysis. *J. Phys. Chem. C* **2009**, *113*, 15068–15072.
- Chou, N. H.; Ross, P. N.; Bell, A. T.; Tilley, T. D. Comparison of Cobalt-based Nanoparticles as Electrocatalysts for Water Oxidation. *ChemSusChem* **2011**, *4*, 1566–1569.
- Liang, Y. Y.; Li, Y. G.; Wang, H. L.; Zhou, J. G.; Wang, J.; Regier, T.; Dai, H. J. Co<sub>3</sub>O<sub>4</sub> Nanocrystals on Graphene as a Synergistic Catalyst for Oxygen Reduction Reaction. *Nat. Mater.* **2011**, *10*, 780–786.
- Smith, R. D. L.; Prevot, M. S.; Fagan, R. D.; Zhang, Z. P.; Sedach, P. A.; Siu, M. K. J.; Trudel, S.; Berlinguette, C. P. Photochemical Route for Accessing Amorphous Metal Oxide Materials for Water Oxidation Catalysis. *Science* **2013**, *340*, 60–63.
- Li, Y. G.; Hsain, P.; Wu, Y. Y. Ni<sub>x</sub>Co<sub>3-x</sub>O<sub>4</sub> Nanowire Arrays for Electrocatalytic Oxygen Evolution. *Adv. Mater.* **2010**, *22*, 1926–1929.
- Trotochaud, L.; Ranney, J. K.; Williams, K. N.; Boettcher, S. W. Solution-Cast Metal Oxide Thin Film Electrocatalysts for Oxygen Evolution. *J. Am. Chem. Soc.* **2012**, *134*, 17253–17261.
- Subbaraman, R.; Tripkovic, D.; Chang, K. C.; Strmcnik, D.; Paulikas, A. P.; Hirunsit, P.; Chan, M.; Greeley, J.; Stamenkovic, V.; Markovic, N. M. Trends in Activity for the Water Electrolyser Reactions on 3d M(Ni,Co,Fe,Mn) hydr(oxy)oxide Catalysts. *Nat. Mater.* **2012**, *11*, 550–557.
- Kanan, M. W.; Nocera, D. G. *In Situ* Formation of an Oxygen-Evolution Catalyst in Neutral Water Containing Phosphate and Co<sup>2+</sup>. *Science* **2008**, *321*, 1072–1075.
- Cobo, S.; Heidkamp, J.; Jacques, P. A.; Fize, J.; Fourmond, V.; Guetaz, L.; Jousset, B.; Ivanova, V.; Dau, H.; Palacin, S.; Fontecave, M.; Artero, V. A Janus Cobalt-Based Catalytic Material for Electro-Splitting of Water. *Nat. Mater.* **2012**, *11*, 802–807.
- Surendranath, Y.; Dinca, M.; Nocera, D. G. Electrolyte-Dependent Electrosynthesis and Activity of Cobalt-Based Water Oxidation Catalysts. *J. Am. Chem. Soc.* **2009**, *131*, 2615–2620.
- Lutterman, D. A.; Surendranath, Y.; Nocera, D. G. A Self-Healing Oxygen-Evolving Catalyst. *J. Am. Chem. Soc.* **2009**, *131*, 3838–3839.
- Zhong, D. K.; Sun, J. W.; Inumaru, H.; Gamelin, D. R. Solar Water Oxidation by Composite Catalyst/ $\alpha$ -Fe<sub>2</sub>O<sub>3</sub> Photoanodes. *J. Am. Chem. Soc.* **2009**, *131*, 6086–6087.
- Zhong, D. K.; Gamelin, D. R. Photoelectrochemical Water Oxidation by Cobalt Catalyst (“Co-Pi”)/ $\alpha$ -Fe<sub>2</sub>O<sub>3</sub> Composite Photoanodes: Oxygen Evolution and Resolution of a Kinetic Bottleneck. *J. Am. Chem. Soc.* **2010**, *132*, 4202–4207.
- Gao, M. R.; Xu, Y. F.; Jiang, J.; Zheng, Y. R.; Yu, S. H. Water Oxidation Electrocatalyzed by an Efficient Mn<sub>3</sub>O<sub>4</sub>/CoSe<sub>2</sub> Nanocomposite. *J. Am. Chem. Soc.* **2012**, *134*, 2930–2933.
- Gao, M. R.; Xu, Y. F.; Jiang, J.; Yu, S. H. Nanostructured Metal Chalcogenides: Synthesis, Modification, and Applications in Energy Conversion and Storage Devices. *Chem. Soc. Rev.* **2013**, *42*, 2986–3017.
- May, K. J.; Carlton, C. E.; Stoerzinger, K. A.; Risch, M.; Suntivich, J.; Lee, Y. L.; Grimaud, A.; Shao-Horn, Y. Influence of Oxygen Evolution during Water Oxidation on the Surface of Perovskite Oxide Catalysts. *J. Phys. Chem. Lett.* **2012**, *3*, 3264–3270.
- Artero, V.; Chavarot-Kerlidou, M.; Fontecave, M. Splitting Water with Cobalt. *Angew. Chem., Int. Ed.* **2011**, *50*, 7238–7266.
- Yin, Q. S.; Tan, J. M.; Besson, C.; Geletii, Y. V.; Musaev, D. G.; Kuznetsov, A. E.; Luo, Z.; Hardcastle, K. I.; Hill, C. L. A Fast Soluble Carbon-Free Molecular Water Oxidation Catalyst Based on Abundant Metals. *Science* **2010**, *328*, 342–345.
- Barroso, M.; Cowan, A. J.; Pendlebury, S. R.; Gratzel, M.; Klug, D. R.; Durrant, J. R. The Role of Cobalt Phosphate in Enhancing the Photocatalytic Activity of  $\alpha$ -Fe<sub>2</sub>O<sub>3</sub> toward Water Oxidation. *J. Am. Chem. Soc.* **2011**, *133*, 14868–14871.
- Gao, M. R.; Liu, S. A.; Jiang, J.; Cui, C. H.; Yao, W. T.; Yu, S. H. *In Situ* Controllable Synthesis of Magnetite Nanocrystals/CoSe<sub>2</sub> Hybrid Nanobelts and Their Enhanced Catalytic Performance. *J. Mater. Chem.* **2010**, *20*, 9355–9361.
- Gao, M. R.; Gao, Q.; Jiang, J.; Cui, C. H.; Yao, W. T.; Yu, S. H. A Methanol-Tolerant Pt/CoSe<sub>2</sub> Nanobelt Cathode Catalyst for Direct Methanol Fuel Cells. *Angew. Chem., Int. Ed.* **2011**, *50*, 4905–4908.
- Gao, M. R.; Lin, Z. Y.; Zhuang, T. T.; Jiang, J.; Xu, Y. F.; Zheng, Y. R.; Yu, S. H. Mixed-Solution Synthesis of Sea Urchin-Like NiSe Nanofiber Assemblies as Economical Pt-Free Catalysts for Electrochemical H<sub>2</sub> Production. *J. Mater. Chem.* **2012**, *22*, 13662–13668.
- Gao, M. R.; Jiang, J.; Yu, S. H. Solution-Based Synthesis and Design of Late Transition Metal Chalcogenide Materials for Oxygen Reduction Reaction (ORR). *Small* **2012**, *8*, 13–27.
- Gao, M. R.; Yao, W. T.; Yao, H. B.; Yu, S. H. Synthesis of Unique Ultrathin Lamellar Mesowire Structured CoSe<sub>2</sub>-Amine (Protonated) Nanobelts in a Binary Solution. *J. Am. Chem. Soc.* **2009**, *131*, 7486–7487.
- Yin, H. J.; Tang, H. J.; Wang, D.; Gao, Y.; Tang, Z. Y. Facile Synthesis of Surfactant-Free Au Cluster/Graphene Hybrids for High-Performance Oxygen Reduction Reaction. *ACS Nano* **2012**, *6*, 8288–8297.
- Tang, H. J.; Yin, H. J.; Wang, J. Y.; Yang, N. L.; Wang, D.; Tang, Z. Y. Molecular Architecture of Cobalt Porphyrin Multilayers on Reduced Graphene Oxide Sheets for High-Performance Oxygen Reduction Reaction. *Angew. Chem., Int. Ed.* **2013**, *52*, 5585–5589.



37. Yin, H. J.; Zhao, S. L.; Wan, J. W.; Tang, H. J.; Chang, L.; He, L. C.; Zhao, H. J.; Gao, Y.; Tang, Z. Y. Three-Dimensional Graphene/Metal Oxide Nanoparticle Hybrids for High-Performance Capacitive Deionization of Saline Water. *Adv. Mater.* **2013**, *25*, 6270–6276.
38. Liang, Y. Y.; Li, Y. G.; Wang, H. L.; Dai, H. J. Strongly Coupled Inorganic/Nanocarbon Hybrid Materials for Advanced Electrocatalysis. *J. Am. Chem. Soc.* **2013**, *245*, 2013–2036.
39. Hummers, W. S.; Offeman, R. E. Preparation of Graphitic Oxide. *J. Am. Chem. Soc.* **1958**, *80*, 1339–1339.
40. Yeh, T. F.; Syu, J. M.; Cheng, C.; Chang, T. H.; Teng, H. S. Graphite Oxide as a Photocatalyst for Hydrogen Production from Water. *Adv. Funct. Mater.* **2010**, *20*, 2255–2262.
41. Fasolino, A.; Los, J. H.; Katsnelson, M. I. Intrinsic Ripples in Graphene. *Nat. Mater.* **2007**, *6*, 858–861.
42. Chen, P.; Xiao, T. Y.; Li, H. H.; Yang, J. J.; Wang, Z.; Yao, H. B.; Yu, S. H. Nitrogen-Doped Graphene/ZnSe Nanocomposites: Hydrothermal Synthesis and Their Enhanced Electrochemical and Photocatalytic Activities. *ACS Nano* **2012**, *6*, 712–719.
43. Liu, S.; Tian, J. Q.; Wang, L.; Zhang, Y. W.; Qin, X. Y.; Luo, Y. L.; Asiri, A. M.; Al-Youbi, A. O.; Sun, X. P. Hydrothermal Treatment of Grass: A Low-Cost, Green Route to Nitrogen-Doped, Carbon-Rich, Photoluminescent Polymer Nanodots as an Effective Fluorescent Sensing Platform for Label-Free Detection of Cu(II) Ions. *Adv. Mater.* **2012**, *24*, 2037–2041.
44. Wang, S. Y.; Zhang, L. P.; Xia, Z. H.; Roy, A.; Chang, D. W.; Baek, J. B.; Dai, L. M. BCN Graphene as Efficient Metal-Free Electrocatalyst for the Oxygen Reduction Reaction. *Angew. Chem., Int. Ed.* **2012**, *51*, 4209–4212.
45. Matsumoto, Y.; Sato, E. Electrocatalytic Properties of Transition-Metal Oxides for Oxygen Evolution Reaction. *Mater. Chem. Phys.* **1986**, *14*, 397–426.
46. Hammer, B.; Nørskov, J. K. Theoretical Surface Science and Catalysis-Calculations and Concepts. *Adv. Catal.* **2000**, *45*, 71–129.
47. Wang, C.; Daimon, H.; Sun, S. H. Dumbbell-like Pt-Fe<sub>3</sub>O<sub>4</sub> Nanoparticles and Their Enhanced Catalysis for Oxygen Reduction Reaction. *Nano Lett.* **2009**, *9*, 1493–1496.
48. Brown, M.; Peierls, R. E.; Stern, E. A. White Lines in X-ray Absorption. *Phys. Rev. B* **1977**, *15*, 738–744.
49. Van, T. T. H.; Pan, C. J.; Rick, J.; Su, W. N.; Hwang, B. J. Nanostructured Ti<sub>0.7</sub>Mo<sub>0.3</sub>O<sub>2</sub> Support Enhances Electron Transfer to Pt: High-Performance Catalyst for Oxygen Reduction Reaction. *J. Am. Chem. Soc.* **2011**, *133*, 11716–11724.
50. Ogawa, S. Magnetic-Properties of 3d Transition-Metal Dichalcogenides with the Pyrite Structure. *J. Appl. Phys.* **1979**, *50*, 2308–2311.